Generative 3D Reconstruction of Martian Surfaces using Monocular Images

Jiarui Cao[1], Rong Huang[1,2], Zhen Ye[1,2], Yusheng Xu[1,2], Xiaohua Tong[1,2]

[1]College of Surveying and Geoinformatics, Tongji University, Shanghai, China
[2] The Shanghai Key Laboratory of Space Mapping and Remote Sensing for Planetary Exploration, Shanghai, China

Keywords: Mars exploration, Digital terrain model, 3D reconstruction, Generative adversarial network (GAN)

Abstract

High-resolution digital terrain models (DEM) are crucial for Mars scientific exploration and engineering demands, such as mission route planning, landing site selection, and topography research. However, DEMs generated based on photogrammetry or photometry suffer from limited stereo coverage and complex generative processes. Therefore, we propose a GAN-based monocular 3D reconstruction method, which utilizes high-resolution monocular orbital images to achieve pixel-level Martian terrain reconstruction. We preprocess the image data and then invert the elevation using the trained generative model. Finally, we recover the absolute scale through post-processing. In this work, we use HiRISE orthorectified images and DEMs with a resolution of 2 m and 0.25 m to validate the effectiveness of our method. We evaluated our method in four areas with different landforms and found that the predicted DEM and HiRISE DEM have height consistency with the root mean square error of about 2 m. This indicates that the proposed GAN-based method has certain effectiveness and generalization and great potential in high-resolution monocular Martian DEM reconstruction.

1. Introduction

High-resolution digital elevation models (DEMs) can reveal the detailed topography and geomorphological features on the surfaces of Mars (Douté and Jiang, 2019), playing an important role in Mars exploration missions and scientific research. They provide crucial support for selecting landing sites (Hedrick et al., 2020) and planning exploration routes (Wu et al., 2021, Wu et al., 2022), and lay a solid foundation for studying the terrestrial planet's evolution and exploring potential life indicators on Mars (Sutton et al., 2022, Qin et al., 2023). Generally, the methods for generating DEMs can be categorized into two major groups: range measurement-based (i.e., laser altimeter) (Abramov and McEwen, 2004), and image-based, including photogrammetry (Hepburn et al., 2019) and photoclinometry (Liu and Wu, 2023). DEMs based on the former method have limited spatial resolution due to the interpolation of a limited number of tracks (e.g. Mars Orbiter Laser Altimeter (MOLA) DEM has a spatial resolution of 463 $m/pixel$ (Neumann et al., 2001)), which is insufficient to satisfy the demands of local fine Martian terrain research.

Image-based methods generate DEMs from high-resolution Mars orbiter images, such as High Resolution Imaging Science Experiment (HiRISE) images (McEwen et al., 2010). Photogrammetric methods recover elevation from the geometric relationship of multi-view remote sensing image data (Shean et al., 2016). However, the coverage of stereo pairs is restricted by the conditions under which the observations are made (McEwen et al., 2023), leading to the limited application of this method (Li et al., 2021). Photometric methods can reconstruct topographic models from single-view images where stereo information is extracted from image intensity variations (Hess et al., 2022). However, due to the presence of an atmosphere on Mars, photoclinometry also has limitations such as complex model building and high production time costs (Jiang et al., 2017). Therefore, it is essential to develop a new method to fully utilize high-resolution monocular orbital images for pixel-level reconstruction of Martian terrain.

In contrast to traditional approaches, deep learning-based methods convert the unconstrained monocular 3D reconstruction problem into a regression problem (Eigen et al., 2014). According to the established network model, deep learning-based methods are mainly categorized into Convolutional Neural Network(CNN)-based approaches and Generative Adversarial Network(GAN)-based approaches (Ming et al., 2021). CNN-based approaches implicitly establish end-to-end mapping relationships between image and depth from a large dataset with sufficient samples (Chen et al., 2021, Chen et al., 2022). Deep neural networks can extract the feature from input monocular images and produce high-resolution reconstruction using depth cues contained in features. GAN-based approaches incorporate adversarial loss to monitor the reconstruction process and improve the accuracy of the reconstructed terrain (Tao et al., 2021b, Liu et al., 2022). Compared to the CNN-based approach, the introduction of the discriminator gives the model a stronger generative capability to represent local details and maintain global consistency (Chen et al., 2018).

Therefore, we propose a GAN-based approach, which transforms the terrain reconstruction problem into the image generation problem and uses the powerful generation capabilities of the well-trained network model to recover height from monocular images. In this study, we select four regions with different surface conditions to test the proposed generative 3D reconstruction strategy and verify the reconstruction results with DEMs (2 $m/pixel$) generated from HiRISE images. In particular, we used higher resolution images (0.25 $m/pixel$) than the training data for experimentation and generated detailed terrain models similar to the resolution of the input images.

2. Method

Our proposed method recovers the pixel-level terrain model with the same resolution as the input monocular high-resolution orbiter imagery through the well-trained generative model. As shown in Fig. 1, the workflow of the proposed generative monocular height reconstruction method consists of three steps.

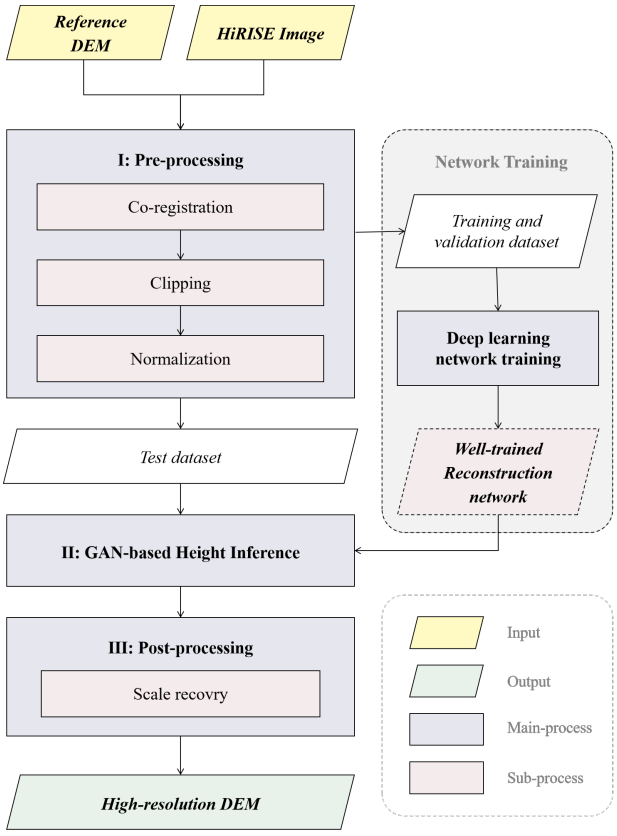

Figure 1. Pipeline of generative monocular height reconstruction method.

First, the HiRISE high-resolution orbiter images are tiled and normalized to preprocess them to meet the input requirements of the network. The preprocessed images are then fed into a trained generator model to reconstruct the relative heights of the images. Finally, the predicted normalized relative heights are stretched to the absolute height scale to obtain a reconstructed high-resolution 3D terrain model.

2.1 Dataset and Pre-processing

The experimental data in this paper are derived from HiRISE Ortho-Rectified Images (ORIs) and DEMs, which have the highest spatial resolution on the surface of Mars at present. Training and validation datasets are based on the publicly accessible image-height dataset generated from 350 pairs of meticulously chosen high-quality HiRISE ORIs and their corresponding DEMs (Tao et al., 2021a). The training dataset comprises 10,000 pairs of HiRISE data, while the validation dataset consists of the other 900 pairs. Each sample within the datasets is standardized to a size of 256×256 pixels, with a spatial resolution of 2 $m/pixel$, so that the influence of the magnitude between different data on the model training impact during training can be eliminated, and the effectiveness of model training can be improved. Considering the machine's memory capacity, the test data must be preprocessed in the same way as the training dataset. First, the geometric disparities between the optical images and the terrain models are rectified through the affine transformation to unify the input data under the same datum. Subsequently, subject to the constraints of machine memory, the input data are uniformly cropped into 256×256 pixel slices. Lastly, the data are normalized using the max-min value to ensure consistency between the test and train datasets, thus enhancing the accuracy of the derived relative elevations.

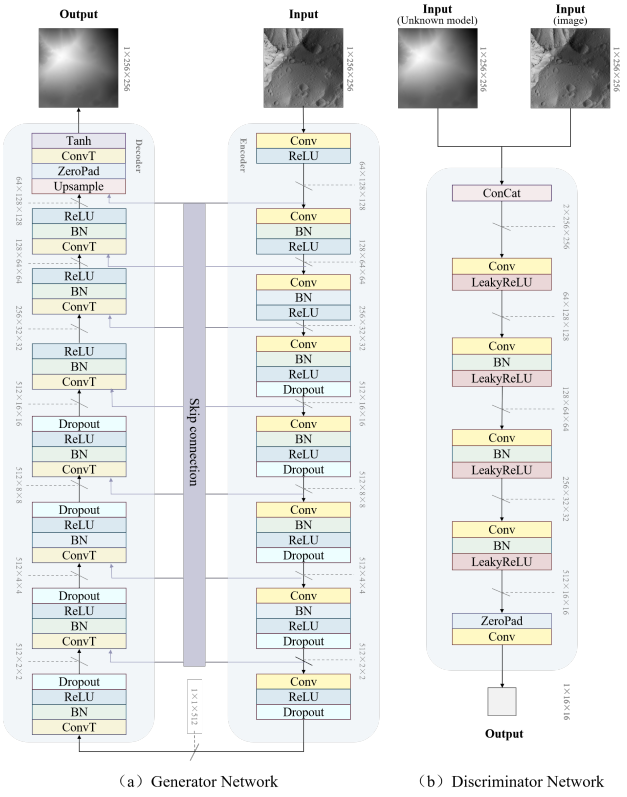

Figure 2. Overview of the generative reconstruction network architecture.

2.2 GAN-based height inference

2.2.1 Network Architecture The GAN-based monocular height reconstruction network is the core component of the entire method. The generative reconstruction network model is shown in Fig. 2. According to the principle of the GAN network (Goodfellow et al., 2020), our network architecture consists of a generator network and a discriminator network.

The generator network adopts a U-Net architecture with symmetric encoder and decoder components (Ronneberger et al., 2015), learning the mapping between optical images and elevation models to generate high-resolution DEMs from input images. The encoder utilizes a series of down-sampling blocks consisting of convolution layers instead of the pooling layers to extract the image's features layer by layer. While the decoder uses a series of up-sampling blocks composed of deconvolution layers and activation functions to decode these high-dimensional features to the size of the input image. Additionally, through skip connections, the features outputted by down-sampling blocks are progressively added to the input of up-sampling blocks, allowing output to contain more fine details from input, providing effective assurance for generating more accurate 3D models.

The discriminator network adopts the principle of PatchGAN (Li and Wand, 2016) to identify the source of the input model and outputs the probability value of the input model from the real dataset. The process is similar to a magnifying glass, which involves dividing the input model into fixed-size blocks, assessing the probability value of each block independently, and then averaging all blocks as the entire image's result. It helps the model capture more precise detailed features while reducing the computational load of the network, effectively improving

the training efficiency of the network.

2.2.2 Loss function In this study, the generator is used to produce predictive terrain models that closely resemble the reference real model to the extent that it can “deceive” the discriminator. At the same time, the discriminator is designed to accurately identify the source of the input model. To make the reconstructed results as close as possible to the real model, the pixel-level height loss and gradient loss are introduced on the basis of the original generation of the adversarial loss. The height loss constrains the differences between the predicted and real models, while the gradient loss maintains the localized terrain features at the pixel level. The basic adversarial losses of the generator and the discriminator are represented as follows:

$$L_{gen} = -E_{H_p \sim P_g}\left[log\left(1 - \mathrm{D}(\mathrm{G}(H_p))\right)\right], \tag{1}$$

$$\begin{aligned} L_{dis} = &- E_{H_{gt} \sim P_{data}}[log \mathrm{D}(H_{gt})] \\ &- E_{H_p \sim P_g}[log(1 - \mathrm{D}(\mathrm{G}(H_p)))], \end{aligned} \tag{2}$$

where H_p is predicted model, H_{gt} is ground truth, and P_{data} is the training dataset distribution. E denotes expectation, $\mathrm{G}(*)$ and $\mathrm{D}(*)$ denote the generator and discriminator, respectively. The stricter Berhu loss is used as the pixel-level elevation loss to better preserve local detail features in the image (Zwald and Lambert-Lacroix, 2012). The formula for Berhu loss is shown below:

$$L_{berhu} = \begin{cases} \frac{1}{n}\sum_{p=1}^{n} \left|H_p - H_{gt}\right|, \left|H_p - H_{gt}\right| \leq \delta \\ \\ \frac{1}{n}\sum_{p=1}^{n} \frac{\left(H_p - H_{gt}\right)^2 + \delta^2}{2\delta}, \left|H_p - H_{gt}\right| > \delta \end{cases} \tag{3}$$

where δ is the threshold value, which is calculated as $\delta = \frac{1}{5} max_p(|H_p - H_{gt}|)$. Gradient loss is introduced to maintain the relationship between pixels and neighboring pixels. The formula for gradient loss is shown below:

$$L_{grad} = \frac{1}{n}\sum_{p=1}^{n}\left[\left(g_x(H_p) - g_x(H_{gt})\right)^2 + \left(g_y(H_p) - g_y(H_{gt})\right)^2\right], \tag{4}$$

where $g_x(H_p)$ and $g_y(H_p)$ represent the gradient values of the predicted DTM model in the x and y-directions, and $g_x(H_{gt})$ and $g_y(H_{gt})$ represent the gradient values of the real DTM model in the x- and y-directions.

In conclusion, The final loss function of the generator consists of a weighted sum of the above three loss terms. Such a loss design helps to improve the performance in terms of generation, making the predicted model as close as possible to the real image, the terrain detail features contained in the input image are increased to generate a more accurate prediction model. The formula for the network losses is given as:

$$Loss_G = \rho Loss_{gen} + \varphi L_{berhu} + \omega L_{grad}, \tag{5}$$

where ρ, φ, and ω are the weight factors of different losses.

2.2.3 Implementation details We implemented this adversarial deep estimation network based on the Pytorch platform (version 1.9.0) and the training process was carried out on the NVIDIA GeForce RTX 3090 GPU. During the training process, we obtain the optimal generator model by alternating the training of the generator and discriminator. The discriminator needs to be fixed when training the generator, while the generator needs to be fixed when training the discriminator. The network is trained for 100 epochs, with a batch size of 10 and an initial learning rate of $2{\times}10^{-4}$. The model is optimized by the standard Adam optimizer, with the hyperparameters set to β_1 = 0.5 and β_2 = 0.999. The generative network's weights of the loss function were set to $\rho = 1$, $\varphi = 10$, and $\omega = 100$, and the hyperparameter values were determined based on empirical values provided in the literature and experimental test results.

2.3 Post-processing

After reconstructing the terrain using GAN-based well-trained models, the relative elevation in the standard scale needs to be stretched to the absolute elevation in the ground scale using the maximum and minimum values provided by the low-resolution reference DEMs. The absolute elevation recovery process can be displayed as follows:

$$\mathrm{H} = (H_{max} - H_{min})\widehat{H} + H_{min} \tag{6}$$

Where H represents the absolute elevation value of the 3D terrain model at the ground scale and $\widehat{H}$ represents the relative elevation value at the standard scale, H_{max} and H_{min} are the maximum and minimum values of the absolute height derived from the corresponding reference terrain models, respectively. Using the aligned low-resolution reference DEMs as the reference for scale recovery, the height range of the predicted DEM is rescaled from [0,1] to $[H_{min}, H_{max}]$, to obtain the well-reconstructed fine 3D terrain model final.

3. Experiments and results

3.1 Reconstruction results for different landforms

We evaluated the generative terrain reconstruction network model in various regions containing different topographic features. Fig. 3 shows the results of the terrain reconstruction of four typical areas with different landforms, including the crater, the crater field, the ridge, and the flat terrain. When the colorized display and hill-shading rendering of the estimated DEM are compared with the HiRISE DEM, the terrain reconstructed using the proposed method is consistent with the reference HiRISE DEM and displays fewer artifacts.

Regions with craters are reconstructed in Fig. 3(a) and Fig. 3(b), with a complete reconstruction of a crater with a diameter of about 200 m and a depth of about 50 m in Fig. 3(a), and the recovery of various craters in different size in Fig. 3(b). Also, Fig. 3(b) indicates that there is no CCD seam in our predicted result, in contrast to the HiRISE DEM. Fig. 3(c) and Fig. 3(d) display the terrain reconstruction results in areas with sharp and gentle terrain relief, respectively, where the edge of the terrain change shown in Fig. 3(c) is the same as the area shown by HiRISE DEM. Overall, the reconstructed terrain is consistent with the HiRISE dem, indicating the reliability of the proposed method.

surface conditions	Crater	Carter Field	Ridge	Flat Terrain
RMSE(m)	1.433	1.315	1.994	1.976

Table 1. Reconstruction error of test areas.

Based on the experiments described above, difference maps are produced to assess the accuracy of our methods. The results are

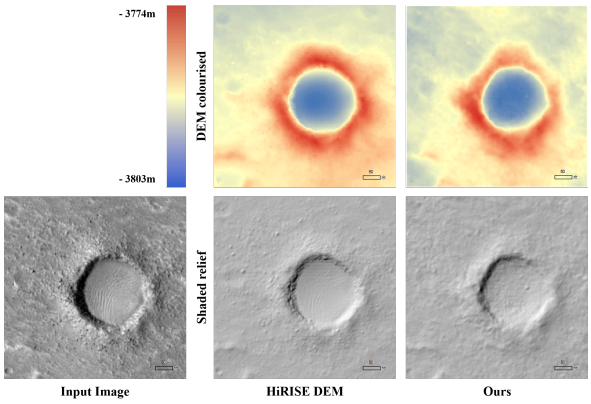

(a) Crater

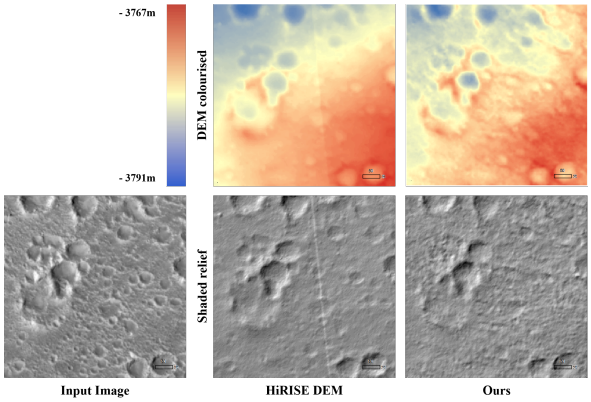

(b) Carter Field

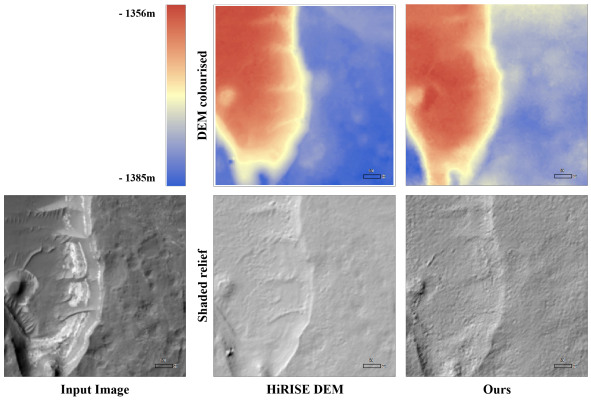

(c) Ridge

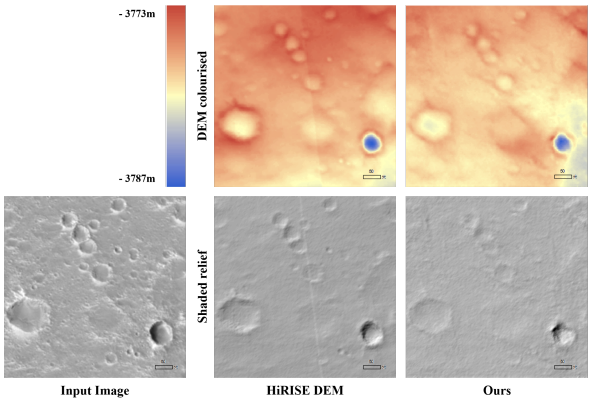

(d) Flat Terrain

Figure 3. Reconstruction results with different surface conditions, colorized and hill-shaded (azimuth: 315°; altitude: 45°; no vertical exaggeration). The first column shows the input HiRISE ORI; the second column shows the HiRISE DEM as a reference; the third column shows our reconstruction results.

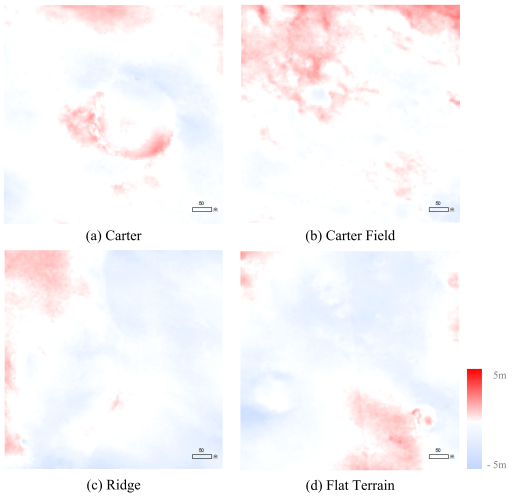

Figure 4. Different maps between predicted DEMs and HiRISE DEMs.

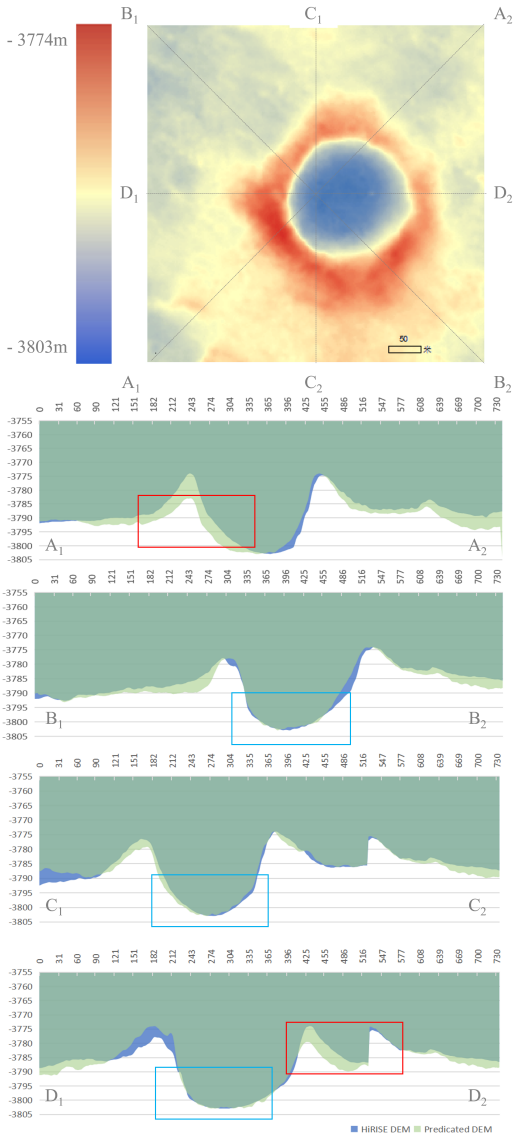

Figure 5. Reconstructed topographic elevation profiles of cratered terrain areas.

presented in Fig. 4 and Table 1. The comparison between the predicted DEMs and the HiRISE DEMs revealed that the elevation differences were generally minor, with an accuracy range of within 2 meters. The discrepancies between the predicted and actual models are not substantial. The accuracy of reconstructing flat areas was slightly lower compared to cratered areas, mainly due to the absence of texture information.

3.2 Profile measurements in different directions

To effectively demonstrate whether the predictive model recovers the terrain trend and evaluate whether the model's accuracy is affected by the light direction, the cratered terrain on Mars displaying the obvious changing trend is chosen. Profiles in different directions are plotted to illustrate the trend of the terrain change of the entire DEM. In Fig. 5, four different directions passing through the craters, A_1A_2, B_1B_2, C_1C_2, and D_1D_2, are taken respectively. The profile measurements of the anticipated DEM and HiRISE DEM were then plotted for each of these directions.

To ensure the comparability of the results, the two DEMs need to be reprojected and aligned in the same geographic space. As can be observed from the profile lines in Fig. 5, both models maintain the same elevation trend in four different directions, especially in the crater floor area showing excellent elevation consistency, such as the area shown by the blue box in the profile. The main terrain differences between the models are reflected in the areas of undulating terrain around the crater, such as the areas shown by the red boxes in the profiles. The height difference exists in the areas affected by light shadowing in profiles A_1A_2 and D_1D_2. The statistical results for the errors in

Profile lines	A_1A_2	B_1B_2	C_1C_2	D_1D_2
MAE(m)	1.879	1.567	1.233	1.345
RMSE(m)	2.567	1.961	1.593	1.676

Table 2. Reconstruction height errors in different directions.

different directions are shown in Table 2. It reveals that the height errors in all four directions are relatively small, and only the error counted for profile A_1A_2 is slightly larger than the other directions, which is consistent with the results shown in Fig. 5. The above results indicate that the predicted model essentially fully recovers the topographic trend with an accuracy of about 2 m. However, the terrain recovery results are still affected by the lighting conditions, especially in the shaded area, which needs to be further studied in the future.

3.3 The attempt at higher resolution terrain reconstruction

The above experiments use 2 $m/pixel$ HiRISE images with the same resolution as the training dataset to recover Martain terrain. To test the adaptability of the model, we attempt to reconstruct the terrain using the HiRISE images with a higher resolution of 0.25 $m/pixel$, and the results are shown in Fig. 6. Compared with the HiRISE DEM generated based on the photogrammetric method, the generative model captures more detailed topographic relief features. The striated texture located at the crater floor is well visible in the hill-shading rendering image of the predicted model, which the photogrammetric-based model cannot reconstruct. It indicates that the proposed method has some generalization capability and a fine terrain model with a similar resolution to the input image can be recovered using

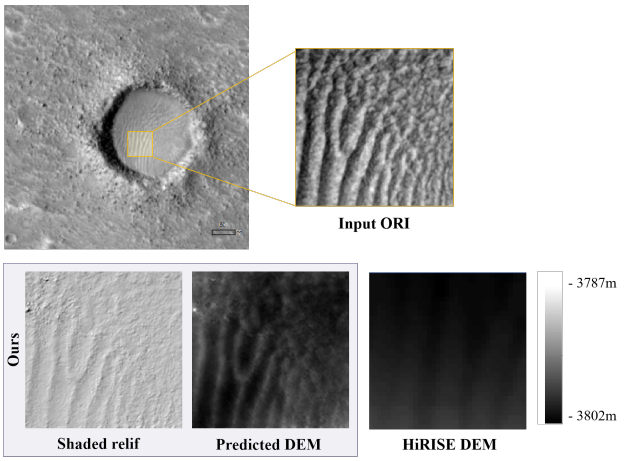

Figure 6. Reconstruction results from 0.25 m/pixel high-resolution image. The first row shows the 0.25 m/pixel HiRISE image and its local zoom details. The purple box in the second row shows the high-resolution predicted DEM and the associated hill-shaded rendering (azimuth: 315°; height: 45°; vertical zoom: 1), and the image outside the purple box in the second row shows the reference 2 m/pixel HiRISE DEM.

our model to process higher resolution optical images. This property can be exploited in the future to generate a larger range of detailed terrain models of the Martian surface.

4. Conclusion

In this paper, we proposed a GAN-based strategy for monocular 3D reconstruction of Martian surfaces. First, we pre-process the image data and then use the trained generator model to invert the elevation. Finally, we recover the absolute scale through post-processing. The network is well-trained with an improved loss function and high-quality datasets. Using the generative power of the GAN model, our approach can generate pixel-level DEMs through monocular 2 $m/pixel$ high-resolution images. With the proposed strategy, in areas with typical landforms of Mars, we can generate the predicted DEM with the RMSE of about 2 m compared with reference HiRISE DEMs. In particular, the strategy can also be applied to 0.25 m resolution HiRISE imagery and obtain more detailed terrain compared to photogrammetry-based DEM, illustrating the effectiveness and applicability of the methods for Mars terrain reconstruction. In the future, we will refine the reconstruction process to obtain finer Martian terrain and apply the pipeline for large-scale mapping.

Acknowledgment

The work described in this paper was supported by the National Key R&D Program of China (2022YFF0504100).

References

Abramov, O., McEwen, A., 2004. An evaluation of interpolation methods for Mars Orbiter Laser Altimeter (MOLA) data. *International Journal of Remote Sensing*, 25(3), 669–676.

Chen, H., Hu, X., Gläser, P., Xiao, H., Ye, Z., Zhang, H., Tong, X., Oberst, J., 2022. CNN-based large area pixel-resolution topography retrieval from single-view LROC NAC images con-

strained with SLDEM. *IEEE Journal of Selected Topics in Applied Earth Observations and Remote Sensing*, 15, 9398–9416.

Chen, R., Mahmood, F., Yuille, A., Durr, N. J., 2018. Rethinking monocular depth estimation with adversarial training. *arXiv preprint arXiv:1808.07528*.

Chen, Z., Wu, B., Liu, W. C., 2021. Mars3DNet: CNN-based high-resolution 3D reconstruction of the Martian surface from single images. *Remote Sensing*, 13(5), 839.

Douté, S., Jiang, C., 2019. Small-scale topographical characterization of the Martian surface with in-orbit imagery. *IEEE Transactions on Geoscience and Remote Sensing*, 58(1), 447–460.

Eigen, D., Puhrsch, C., Fergus, R., 2014. Depth map prediction from a single image using a multi-scale deep network. *Advances in neural information processing systems*, 27.

Goodfellow, I., Pouget-Abadie, J., Mirza, M., Xu, B., Warde-Farley, D., Ozair, S., Courville, A., Bengio, Y., 2020. Generative adversarial networks. *Communications of the ACM*, 63(11), 139–144.

Hedrick, G., Ohi, N., Gu, Y., 2020. Terrain-aware path planning and map update for mars sample return mission. *IEEE Robotics and Automation Letters*, 5(4), 5181–5188.

Hepburn, A. J., Holt, T., Hubbard, B., Ng, F., 2019. Creating HiRISE digital elevation models for Mars using the open-source ames stereo pipeline. *Geoscientific Instrumentation, Methods and Data Systems*, 8(2), 293–313.

Hess, M., Tenthoff, M., Wohlfarth, K., Wöhler, C., 2022. Atmospheric Correction for High-Resolution Shape from Shading on Mars. *Journal of Imaging*, 8(6), 158.

Jiang, C., Douté, S., Luo, B., Zhang, L., 2017. Fusion of photogrammetric and photoclinometric information for high-resolution DEMs from Mars in-orbit imagery. *ISPRS Journal of Photogrammetry and Remote Sensing*, 130, 418–430.

Li, C., Wand, M., 2016. Precomputed real-time texture synthesis with markovian generative adversarial networks. *Computer Vision–ECCV 2016: 14th European Conference, Amsterdam, The Netherlands, October 11-14, 2016, Proceedings, Part III 14*, Springer, 702–716.

Li, Z., Wu, B., Liu, W. C., Chen, Z., 2021. Integrated photogrammetric and photoclinometric processing of multiple HRSC images for pixelwise 3-D mapping on Mars. *IEEE Transactions on Geoscience and Remote Sensing*, 60, 1–13.

Liu, W. C., Wu, B., 2023. Atmosphere-aware photoclinometry for pixel-wise 3D topographic mapping of Mars. *ISPRS Journal of Photogrammetry and Remote Sensing*, 204, 237–256.

Liu, Y., Wang, Y., Di, K., Peng, M., Wan, W., Liu, Z., 2022. A Generative Adversarial Network for Pixel-Scale Lunar DEM Generation from High-Resolution Monocular Imagery and Low-Resolution DEM. *Remote Sensing*, 14(21), 5420.

McEwen, A., Byrne, S., Hansen, C., Daubar, I., Sutton, S., Dundas, C., Bardabelias, N., Baugh, N., Bergstrom, J., Beyer, R. et al., 2023. The high-resolution imaging science experiment (HiRISE) in the MRO extended science phases (2009–2023). *Icarus*, 115795.

McEwen, A. S., Banks, M. E., Baugh, N., Becker, K., Boyd, A., Bergstrom, J. W., Beyer, R. A., Bortolini, E., Bridges, N. T., Byrne, S. et al., 2010. The high resolution imaging science experiment (HiRISE) during MRO’s primary science phase (PSP). *Icarus*, 205(1), 2–37.

Ming, Y., Meng, X., Fan, C., Yu, H., 2021. Deep learning for monocular depth estimation: A review. *Neurocomputing*, 438, 14–33.

Neumann, G. A., Rowlands, D. D., Lemoine, F. G., Smith, D. E., Zuber, M. T., 2001. Crossover analysis of Mars orbiter laser altimeter data. *Journal of Geophysical Research: Planets*, 106(E10), 23753–23768.

Qin, X., Ren, X., Wang, X., Liu, J., Wu, H., Zeng, X., Sun, Y., Chen, Z., Zhang, S., Zhang, Y. et al., 2023. Modern water at low latitudes on Mars: Potential evidence from dune surfaces. *Science advances*, 9(17), eadd8868.

Ronneberger, O., Fischer, P., Brox, T., 2015. U-net: Convolutional networks for biomedical image segmentation. *Medical image computing and computer-assisted intervention–MICCAI 2015: 18th international conference, Munich, Germany, October 5-9, 2015, proceedings, part III 18*, Springer, 234–241.

Shean, D. E., Alexandrov, O., Moratto, Z. M., Smith, B. E., Joughin, I. R., Porter, C., Morin, P., 2016. An automated, open-source pipeline for mass production of digital elevation models (DEMs) from very-high-resolution commercial stereo satellite imagery. *ISPRS Journal of Photogrammetry and Remote Sensing*, 116, 101–117.

Sutton, S. S., Chojnacki, M., McEwen, A. S., Kirk, R. L., Dundas, C. M., Schaefer, E. I., Conway, S. J., Diniega, S., Portyankina, G., Landis, M. E. et al., 2022. Revealing active Mars with HiRISE digital terrain models. *Remote Sensing*, 14(10), 2403.

Tao, Y., Muller, J.-P., Xiong, S., Conway, S. J., 2021a. MADNet 2.0: Pixel-scale topography retrieval from single-view orbital imagery of Mars using deep learning. *Remote Sensing*, 13(21), 4220.

Tao, Y., Xiong, S., Conway, S., Muller, J.-P., Guimpier, A., Fawdon, P., Thomas, N., Cremonese, G., 2021b. Rapid Single Image-Based DTM Estimation from ExoMars TGO CaSSIS Images Using Generative Adversarial U-Nets. *Remote Sensing*, 13, 2877.

Wu, B., Dong, J., Wang, Y., Li, Z., Chen, Z., Liu, W. C., Zhu, J., Chen, L., Li, Y., Rao, W., 2021. Characterization of the Candidate Landing Region for Tianwen-1—China’s First Mission to Mars. *Earth and Space Science*, 8(6), e2021EA001670.

Wu, B., Dong, J., Wang, Y., Rao, W., Sun, Z., Li, Z., Tan, Z., Chen, Z., Wang, C., Liu, W. C. et al., 2022. Landing site selection and characterization of Tianwen-1 (Zhurong rover) on Mars. *Journal of Geophysical Research: Planets*, 127(4), e2021JE007137.

Zwald, L., Lambert-Lacroix, S., 2012. The berhu penalty and the grouped effect. *arXiv preprint arXiv:1207.6868*.